



The 2016 Kaikōura earthquake: Simultaneous rupture of the subduction interface and overlying faults



Teng Wang ^a, Shengji Wei ^{a,b,*}, Xuhua Shi ^a, Qiang Qiu ^c, Linlin Li ^a, Dongju Peng ^a, Ray J. Weldon ^{a,d}, Sylvain Barbot ^{a,b}

^a Earth Observatory of Singapore, Nanyang Technological University, Singapore

^b Asian School of the Environment, Nanyang Technological University, Singapore

^c School of Earth and Environment, University of Leeds, United Kingdom

^d Department of Geological Science, University of Oregon, United States

ARTICLE INFO

Article history:

Received 2 August 2017

Received in revised form 22 October 2017

Accepted 26 October 2017

Available online xxxx

Editor: P. Shearer

Keywords:

finite rupture model

strong motion

teleseismic waveform modeling

3D surface deformation

tsunami

SAR/InSAR GPS

ABSTRACT

The distribution of slip during an earthquake and how it propagates among faults in the subduction system play a major role in seismic and tsunami hazards, yet they are poorly understood because offshore observations are often lacking. Here we derive the slip distribution and rupture evolution during the 2016 M_w 7.9 Kaikōura (New Zealand) earthquake that reconcile the surface rupture, space geodetic measurements, seismological and tsunami waveform records. We use twelve fault segments, with eleven in the crust and one on the megathrust interface, to model the geodetic data and match the major features of the complex surface ruptures. Our modeling result indicates that a large portion of the moment is distributed on the subduction interface, making a significant contribution to the far field surface deformation and teleseismic body waves. The inclusion of local strong motion and teleseismic waveform data in the joint inversion reveals a unilateral rupture towards northeast with a relatively low averaged rupture speed of ~ 1.5 km/s. The first 30 s of the rupture took place on the crustal faults with oblique slip motion and jumped between fault segments that have large differences in strike and dip. The peak moment release occurred at ~ 65 s, corresponding to simultaneous rupture of both plate interface and the overlying splay faults with rake angle changes progressively from thrust to strike-slip. The slip on the Papatea fault produced more than 2 m of offshore uplift, making a major contribution to the tsunami at the Kaikōura station, while the northeastern end of the rupture can explain the main features at the Wellington station. Our inversions and simulations illuminate complex up-dip rupture behavior that should be taken into consideration in both seismic and tsunami hazard assessment. The extreme complex rupture behavior also brings new challenges to the earthquake dynamic simulations and understanding the physics of earthquakes.

© 2017 The Author(s). Published by Elsevier B.V. This is an open access article under the CC BY-NC-ND license (<http://creativecommons.org/licenses/by-nc-nd/4.0/>).

1. Introduction

At 12:03 am local time, on November 14th, 2016, a moment magnitude (M_w) 7.8 (USGS) earthquake struck the Kaikōura region of South Island, New Zealand. The earthquake occurred at a complicated portion of the Australian-Pacific plate boundary, where the motion between the two plates decreases southwestward, and the azimuth changes from trench-normal to trench-parallel along the 3000 km southward-developing subduction system (Litchfield et al., 2014) (Fig. 1 inset). The epicenter of the earthquake (Fig. 1a

and inset) is located at the southern end of the subducting system (Barker et al., 2009; Eberhart-Phillips and Bannister, 2010; Williams et al., 2013). The 2016 Kaikōura earthquake was not unexpected, given its plate boundary location and the historical seismicity, yet it exhibited exceptional complexity. This complexity was initially reflected by the significant non-double-couple centroid moment tensor (CMT) solutions from the USGS (USGS, 2016) and GCMT (Ekstrom et al., 2012) (Fig. 1). Subsequently, field and aerial observations and satellite radar images acquired immediately after the earthquake showed that the quake produced one of the most complex surface ruptures ever recorded (Clark et al., 2017; Litchfield et al., 2017; Stirling et al., 2017). Although the epicenter is ~ 50 km inland from the coast, the accompanying tsunami caused up to 5 m of run-ups at Goose Bay, on the Banks Peninsula, to the south of the epicenter and was well recorded by

* Corresponding author at: Earth Observatory of Singapore, Nanyang Technological University, Singapore.

E-mail address: shjwei@ntu.edu.sg (S. Wei).

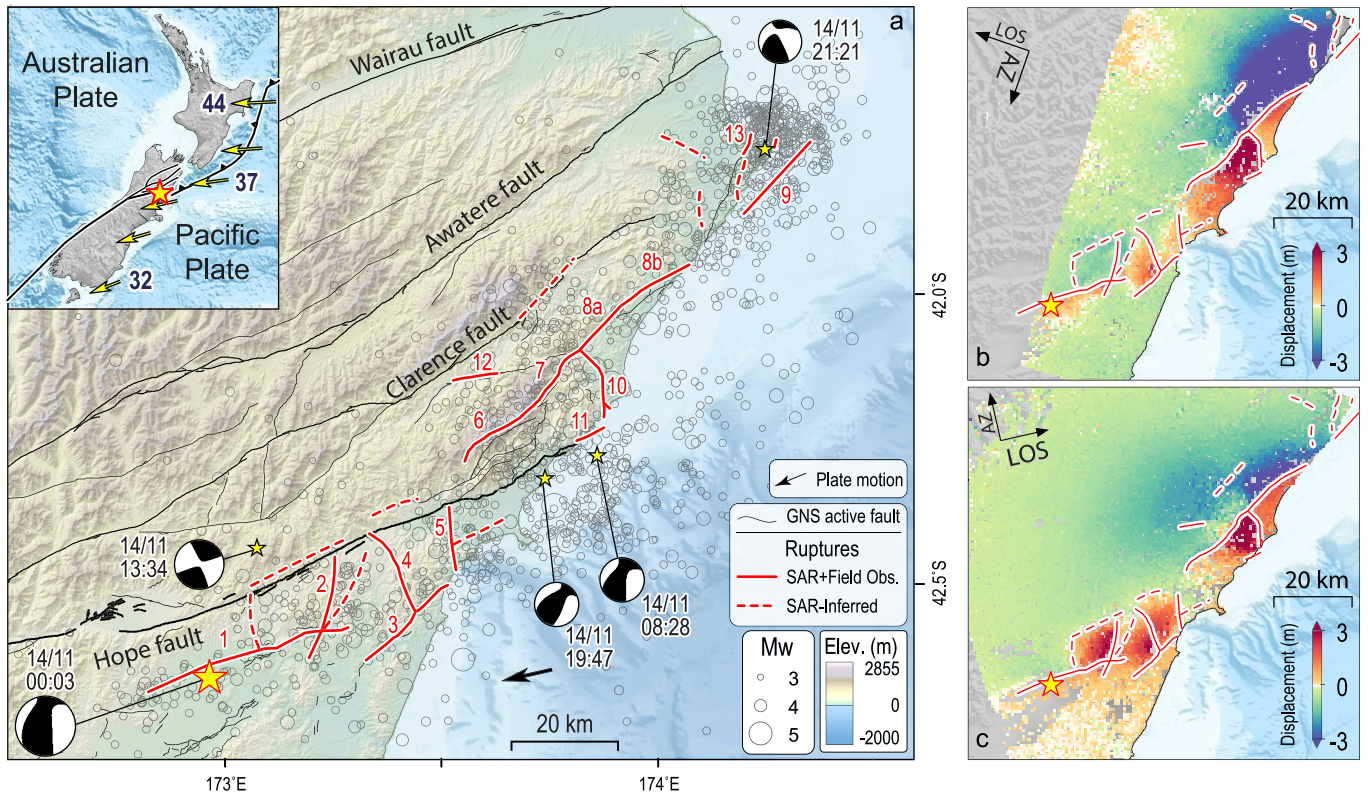


Fig. 1. Setting and surface ruptures of the Kaikōura earthquake. The inset in **a** shows a simplified plate boundary of New Zealand, with arrows representing the relative motion of the Pacific Plate with respect to the Australian Plate derived from the NUVEL 1A model (Argus and Gordon, 1991), the numbers next to the arrows show the plate motion rates in mm/yr. The Marlborough Fault System includes four major faults with names in black. The gray circles show aftershocks with moments larger than 3 within one week after the main shock. Focal mechanisms of earthquakes with magnitudes larger than 6 are from global CMT (Ekstrom et al., 2012). **b** shows image offsets along the satellite's direction of motion derived from ALOS-2 data. Warm colors represent southward movement. **c** shows image offsets in the satellite line-of-sight direction derived from Sentinel-1 data. Warm color indicate mainly uplift. The mapped ruptures are: 1 – Humps fault, 2 – Leader fault, 3 – Hundalee fault, 4 – Stone Jug fault, 5 – Whites fault, 6 – Upper Kowhai fault, 7 – Jordan Thrust fault, 8a – Kekerengu fault (SW), 8b – Kekerengu fault (NE), 9 – Needles fault, 10 – Papatea fault, 11 – Hope fault, 12 – Fidget fault, 13 – London Hills fault. The fault traces are based on Langridge et al. (2016), Litchfield et al. (2014).

many tide gauges located along the east coast of New Zealand (Lane et al., 2017; Power et al., 2017) (Fig. S1). The seismic and tsunami hazard due to such a complex rupture cannot be faithfully characterized based on a more typical single-fault rupture scenario (Hamling et al., 2017; Shi et al., 2017).

Dense geodetic measurements and strong motion seismometers onshore provided valuable near-field observations to study slip partitioning in the up-dip portion of the subduction system, as the coastline is particularly close to the trench (<50 km). Preliminary seismological analysis shows that the mechanism of the mainshock was oblique thrust (Kaiser et al., 2017). Hamling et al. (2017) derived a static slip model with more than 10 fault segments using GPS and InSAR data. The surface displacement can be fitted reasonably well from their preferred model with most of the slip occurred on crustal faults, yet they have difficulties in simulating the observed tsunami waveforms. This is partially because they did not use a fault segment for the Papatea fault as they considered the associated deformation was inelastic and they could not fit it. Hollingsworth et al. (2017) used optical satellite imagery and teleseismic data to analyze the earthquake rupture process. Their rupture model, which was derived with only seismic data assuming a two-segment fault geometry, shows a source duration of ~100 s with unilateral rupture to the northeast and most of the slip occurring on the subduction interface. Their model is similar to the result of multiple-point source models derived from the long-period teleseismic data (Duputel and Rivera, 2017), and the result from the back-projection analysis (Zhang et al., 2017). Combining teleseismic seismological and tsunami records, Bai et al. (2017) and Furlong and Herman (2017) propose that the megath-

rust fault accounts for a major source of the tsunami. Among the published models, the seismological and tsunami modeling prefer the involvement of the slip on the subduction interface, while geodetic data and field observations prefer shallow crustal faulting as the dominating mechanism for this event. By jointly inverting seismological and geodetic data, Cesca et al. (2017) derive a three-fault-segment model with large slip occurred on a shallow dipping thrust fault connecting two shallow strike-slip faults. They interpret this thrust fault as a crustal fault rather than the interface based on the depth distribution of relocated aftershocks, which are mostly above this thrust fault. Previous studies have been hitherto limited to only one or two types of datasets, however, to date, there is no rupture model that can completely reconcile all available datasets. Here we exploit all available datasets from near-field to far-field and both static and dynamic observations, to draw a complete picture of the slip initiation, propagation and distribution during this extraordinary event. From our rupture model, we explain how the interaction of the subduction interface at depth and the overlying faults produced the abrupt coastal uplift, which triggered the tsunami that hit the coastal area.

2. Three-dimensional coseismic displacement

We mapped ruptures and derived high-resolution three-dimensional (3D) coseismic displacement, using synthetic aperture radar (SAR) images from eight independent tracks (Fig. S1 and Table S1) acquired from the Japanese ALOS-2 and European Sentinel-1A/B satellites. To map the ruptures, we calculated pixel offsets of SAR images by tracking amplitude features between pre- and

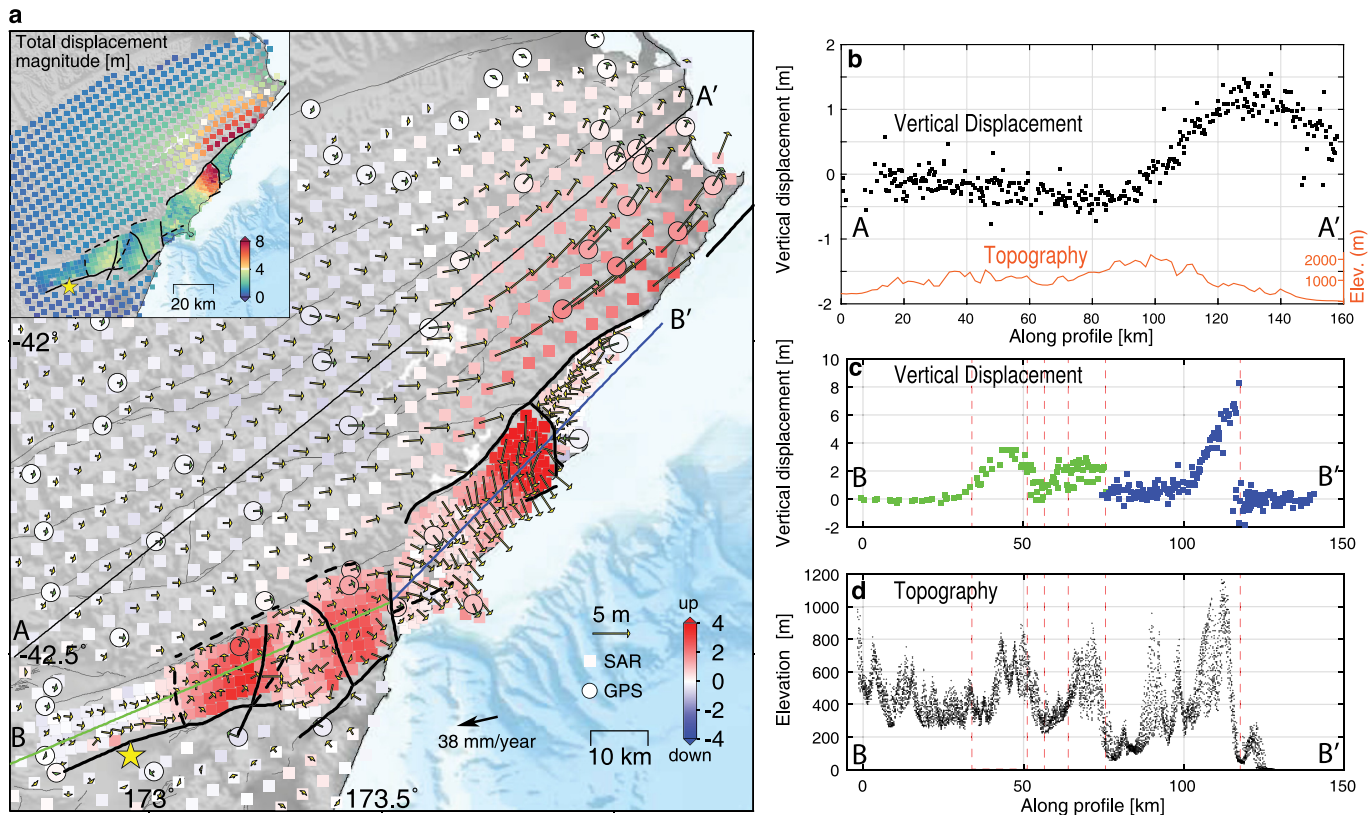


Fig. 2. Three-dimensional coseismic displacement. **a.** Displacement derived by combining Sentinel-1A/B and ALOS-2 SAR image offsets and plotted with GPS data. Significant ruptures are in black. The inset shows the magnitude of total surface displacement. **b** and **c** show vertical displacement along profiles AA' (inland) and BB' (coast), respectively. The orange line in **b** shows the topography along profile AA'. **d** shows the topography within a 1 km-wide swath along profile BB'. Red dashed lines in **c** and **d** show locations where the profiles intersect surface ruptures.

post-earthquake images, and then calculated the 3D displacement by combining SAR image offsets from five independent tracks with the highest quality (Fig. S1, see supplement for more details). Discontinuities in the pixel-offset data allow us to identify more than 20 surface ruptures, thirteen of which are consistent with available field observations by the Institute of Geological and Nuclear Sciences (GNS) in New Zealand (Clark et al., 2017; Litchfield et al., 2017; Stirling et al., 2017) (Fig. 1). The mapped surface ruptures and the 3D displacements reveal that the rupture propagated among numerous fault segments with a wide range of orientations (from approximately parallel to the plate motion to perpendicular to the plate motion), dip angles (from nearly vertical to $\sim 45^\circ$) and slip styles (strike-slip, thrust and normal faulting), thus exhibiting, arguably, the most complex rupture behaviors ever recorded in a single event (Hamling et al., 2017; Shi et al., 2017; Kaiser et al., 2017).

Examination of the SAR imagery reveals that the largest horizontal displacement at the surface occurred on the northern portion of the Kekerengu fault, while the largest uplift occurred south of the Jordan Thrust fault (Fig. 2a). To the north of the Kekerengu fault, the slip was predominantly a smoothly-varying right-lateral horizontal motion with up to 4 m of uplift. As we move from west to the east, the strike of the horizontal motion gradually rotates from almost parallel to the WSW-directed plate motion, to parallel to the NE-striking Kekerengu fault, and finally to parallel to the NNE-striking offshore Needles fault (Litchfield et al., 2014). The vertical deformation along profile AA' (Fig. 2b) to the northwest of the main rupture area exhibits a bell-shaped uplift pattern with width of ~ 100 km in the east, followed by slight subsidence in the west (Fig. 2b). The uplift along this profile corresponds to a region with low topography, while the subsidence occurred in an area of relatively high topography (Fig. 2b), repre-

senting a vertical displacement pattern observed during some megathrust earthquakes, e.g., the 2011 M_w 9.0 Tohoku earthquake in Japan (Takada and Fukushima, 2013) and the 2015 M_w 7.8 Gorkha earthquake in Nepal (Avouac et al., 2015; Elliott et al., 2016). In contrast, surface displacements farther to the southeast are much more complex (BB' profile in Fig. 2c). To the west of the Papatea fault, a 15-by-100-km² area was uplifted and segmented by many previously unidentified NW-SE-orientated faults, forming at least three major blocks. The largest uplift (~ 8 m) occurred within the easternmost block at the triple-junction that connects the Jordan Thrust, the Kekerengu and the Papatea faults. The BB' profile also shows that the vertical displacement rapidly decreases away from the rupture (Fig. 2c), very different from the pattern to the north (Fig. 2b). Along the coast, the vertical displacement pattern is broadly correlated with the topography, where mountain ranges with a series of high peaks can be found (Fig. 2d), suggesting repeated coseismic uplifts during historical events. Similar geomorphic signatures have been documented along the east coast to the north (Mountjoy and Barnes, 2011).

The observed surface displacement is highly unusual in several respects. Firstly, the earthquake initiated from the Humps fault (closest to the epicenter) (Kaiser et al., 2017) rather than the fastest-slipping Hope fault that is just 10 km to the north and accommodates about half of the relative plate motion (Langridge et al., 2016; Van Dissen and Yeats, 1991). The rupture then propagated towards the northeast, activating several faults that are perpendicular to the Hope fault, again rather than the Hope fault itself (Hamling et al., 2017; Shi et al., 2017; Kaiser et al., 2017). Secondly, surface ruptures are highly segmented with large gaps (~ 15 km wide) between rupture segments, such as between the Humps and Hundalee faults, and between the Whites fault and the Upper Kowhai fault (Hamling et al., 2017; Shi et al., 2017;

Litchfield et al., 2017) (Fig. 1). Thirdly, surface motions across several faults cannot be explained by any strike-slip, reverse or normal faulting mechanism alone. For example, both the hanging wall and the foot wall of the Jordan Thrust fault were uplifted during the earthquake, with the foot wall uplifted more than the hanging wall. Additionally, a ~4 m uplift took place south of the Hope fault with little horizontal motion, though the Hope fault is predominately a strike-slip fault that dips almost vertically (Van Dissen and Yeats, 1991). Finally, the vertical displacements are positively correlated with topography along the coast but are negatively correlated with topography farther inland (Fig. 2b-d), suggesting opposite coseismic contributions to the shaping of the Earth's surface.

3. Finite rupture process

To better understand such a complex coseismic displacement pattern, we derived a finite rupture model that reconciles most of the seismic and geodetic datasets (see supplement for more details). We used rectangular fault segments to approximate the ruptured faults, and divided each fault segment into smaller fault patches. We first conducted a static inversion using the geodetic data, to determine the fault geometry and slip distribution. Taking into account the geologic setting (Langridge et al., 2016; Litchfield et al., 2014; Van Dissen and Yeats, 1991), surface rupture geometry constrained from GNS field observations (Clark et al., 2017; Litchfield et al., 2017; Stirling et al., 2017) and our high-resolution geodetic data (GPS and SAR imagery), we chose 12 fault segments to approximate this complex earthquake. We determined the average strike and dip of these 12 segments from previous geological studies (Langridge et al., 2016; Litchfield et al., 2014; Van Dissen and Yeats, 1991), and adjusted those parameters by trial-and-error tests to minimize the misfit between modeled and observed coseismic displacement. The preferred fault segment geometry can be found in the Table S2. To model the geodetic data, particularly the far-field observations, we have to place a 25° dipping fault segment beneath the rupture area where the subduction interface was clearly imaged by seismic reflection data and seismicity (Barker et al., 2009; Williams et al., 2013). We tested model configurations with and without slip on the plate interface (Fig. 3b, Segment S). Our tests indicate that model fits are significantly improved with the inclusion of slip on the plate interface, especially in the fit of the far-field static GPS data (Fig. 4a and Fig. S5). Slip on the shallow crustal faults primarily contributed to the near-field displacement, best derived from SAR imagery (Fig. 4b).

With fault geometry determined by geodetic and geologic data, we then resolved the timing of the rupture on each segment by jointly inverting the geodetic measurements, local strong motion and teleseismic P and SH-waves. We parameterized the model as the distribution of slip (characterized by rake and magnitude of slip on each subfault), the rupture velocity and the rise time (Ji et al., 2002). Our preferred joint inversion model yields excellent fits to the geodetic data (Fig. 4, Fig. S2), teleseismic waveform (Fig. S3) and strong motion data (Fig. S4). The total moment of the joint inversion model is 1.04×10^{21} Nm (M_w 7.94), calculated by summing the contribution from each fault segment. The equivalent moment tensor (Fig. 3a) is almost identical with the W-phase from USGS (USGS, 2016) and GCMT (Ekstrom et al., 2012) solutions, except that our moment magnitude is slightly larger, which is not unexpected given that a finite fault model has a more detailed slip distribution than the point source CMT solutions. Moreover, early afterslip is included in SAR images and campaign GPS data, which were acquired a few days after the earthquake (Hamling et al., 2017). The decomposition of the contribution from different fault segments to the moment tensor (Fig. 3a) again indicates that complex fault geometry and rupture processes on both the plate interface and overlying faults are required to produce such a

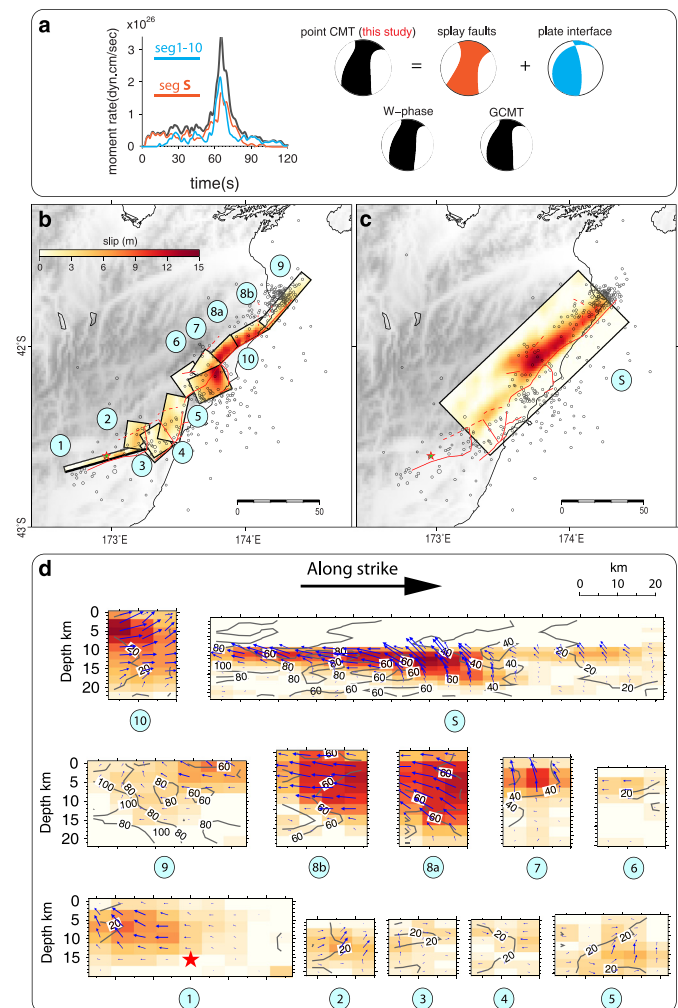


Fig. 3. Slip model derived from teleseismic, strong-motion and geodetic data. **a.** Moment-rate function of the joint inversion model (black line); blue and red colors indicate the contribution from the rupture on the plate interface and overlying faults, respectively. The decomposition of the equivalent moment tensor is shown to the right, along with W-phase and GCMT solutions. **b-c.** Map views of the slip distributions for fault segments 1–10 and segment S. **d.** Depth profiles of slip distribution of 12 fault segments. The hypocenter is indicated by the red star in segment 1. The contours show the rupture time relative to the origin time.

strong non-double-couple component in the CMT solution. In our preferred slip model, almost half (~45%) of the total moment was released on the subduction interface, distributed mostly beneath the Kekerengu and the Jordan Thrust faults (Fig. 3c).

The joint inversion model shows that rupture initiated with a strike-slip motion at 15 km depth on the Humps fault, dipping 80° to the north (Fig. 3, fault segment 1), and unilaterally propagated to the northeast. The rupture on this segment ended with a transpressional motion with peak slip of ~8 m, resulting in a major contribution to the uplift south of the Hope fault (Fig. 2a). About 15 s after the event started, the rupture propagated to the Hundalee fault, and two previously un-identified faults (fault segments 2–4). The slip magnitudes on these fault segments were relatively small, with characteristic transpressional motion. Between 22 s and 35 s after the beginning of the event, the rupture passed through an unknown SW-NE strike-slip fault (fault segment 5), and then ruptured the upper Kowhai fault (fault segment 6). At about 40 s into the event, rupture on the shallower-dipping (45°) Jordan Thrust fault (fault segment 7) was triggered; note that the motion of this fault segment in our model is almost pure thrust, consistent with the geological observations (Van Dissen and Yeats, 1991). The

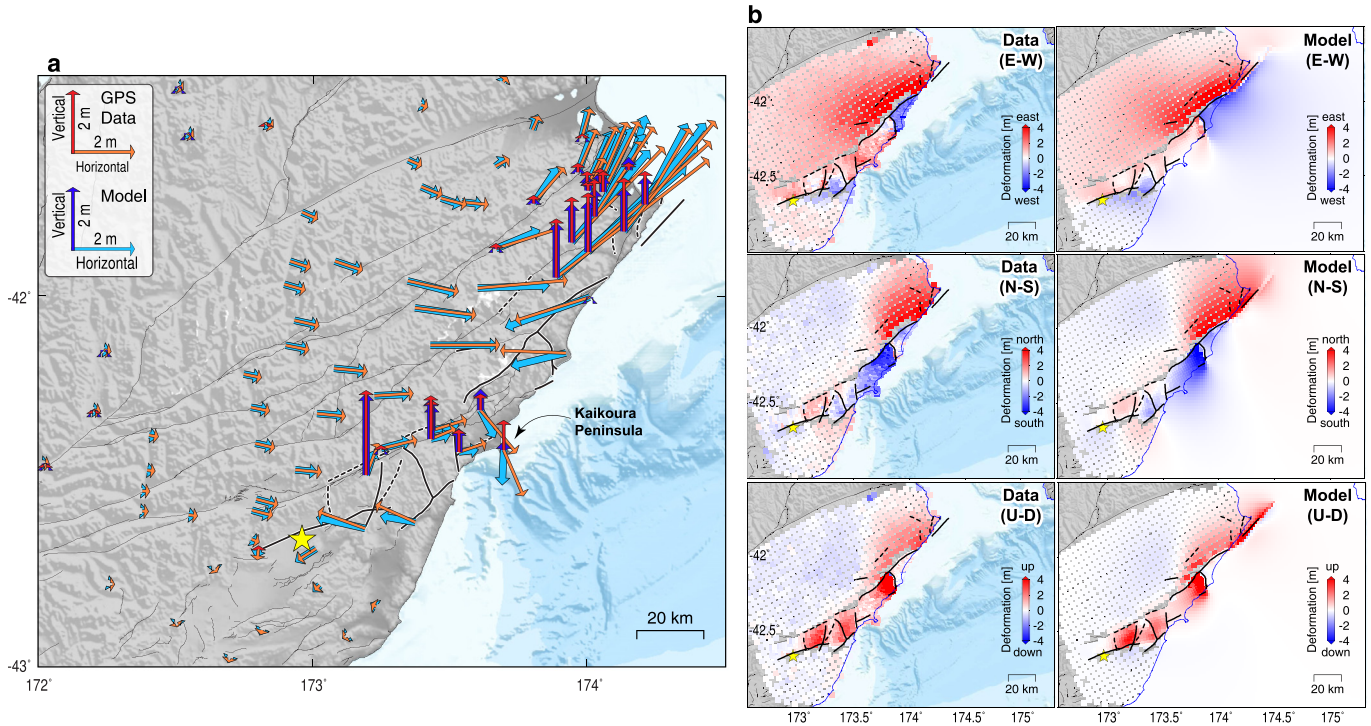


Fig. 4. Fitting of the geodetic data. **a.** Fit to the static GPS offsets, both for vertical and horizontal components from the joint inversion of geodetic and seismic datasets. **b.** Comparison between the 3D surface deformation derived from the geodetic data (left panels) and that computed from our preferred slip model (right panels).

rupture on the Papatea fault (fault segment 10) took place at almost the same time of the rupture on the Jordan Thrust fault (fault segment 7), producing the largest uplift during the earthquake (Fig. 4b). The rupture then propagated to the Kekerengu fault (fault segments 8a and 8b) with dip angles steepening from 60° to 70° , while the style of slip progressively transformed from pure thrust to pure strike-slip. The peak moment release on these high-dipping angle strike-slip fault segments occurred at about 65 s, coincident with the largest slip of about 15 m on the Kekerengu fault (fault segment 8a). This model result corresponds to the largest horizontal offset (>11 m) observed both in the field and in the geodetic data on this fault (Clark et al., 2017; Hamling et al., 2017; Litchfield et al., 2017). Below these shallow crustal faults, rupture on the plate interface was triggered about 20 s after the event began and propagated unilaterally northeastward along the coast. Large slip on the interface (Fig. 3 fault segment S) occurred beneath the Jordan Thrust fault and extended about 60 km, parallel to the rupture on the shallow crustal faults. More interestingly, the fault motion on the interface also presents a progressive transformation from pure thrust (beneath the upper Kowhai fault and Jordan Thrust fault, fault segment 7) to almost pure strike-slip (beneath the Kekerengu fault, fault segment 6). The moment-rate function peaks at 65 s, with simultaneous maximum contributions from the plate interface and shallow crustal faults (Fig. 3a). The consistency of the spatial distribution and the moment-rate function between the shallow crustal fault and the plate interface indicates that the shallow crustal fault system is attached to the plate interface, likely splaying off the subducting slab.

Evidence of coseismic rupture on both the shallow crustal faults and the plate interface also come from teleseismic and strong motion data, as these datasets have different sensitivity owing to their different sampling of the radiated seismic energy (Fig. S6). The relative contributions of slip along the plate interface and the overlying faults (Fig. 5) show that the rupture on the plate interface mainly contributed to the largest pulse in the teleseismic P waves at ~ 70 s, while the shallower ruptures contributed more in fitting the first 40 s of teleseismic P-waves and the local strong motion

waveforms. The difference in the amplitude ratio between the first 40 s and the peak amplitude (at ~ 70 s) in the teleseismic P-waves (e.g. PMSA vs. COCO station in Fig. 5) also indicates that the radiation pattern at the beginning of the rupture is different from that during the peak rupture, requiring a complex fault geometry and rupture (Wei et al., 2011). The averaged rupture speed of the earthquake is determined in a grid search manner (Fig. S7), which shows a preferred value of ~ 1.5 km/s, in agreement with the back-projection results (Zhang et al., 2017). The slow averaged rupture speed also implies complex triggering between fault segments, in contrast to super-shear rupture events that usually show much simpler fault geometries (Bouchon and Vallee, 2003). The extremely complex geometry and time evolution of the Kaikoura earthquake challenge our understanding of the physics of earthquake ruptures. The surface rupture is highly segmented, particularly in the region near the epicenter where several rupture gaps are up to 15 km wide (Fig. 1 and 6), much larger than are usually found in other observations (Wesnousky, 2006) and dynamic modeling of strike-slip fault (Harris and Day, 1999) or megathrust earthquakes (Qiu et al., 2016). This observation clearly demonstrates difficulty in understanding how rupture jumps from one fault to another within extreme complex fault systems.

Comparing with published models derived from geodetic data (e.g., Hamling et al., 2017), our model has much more slip on the subduction plate interfaces; this feature is consistent with some models derived from seismological data (e.g., Hollingsworth et al., 2017; Duputel and Rivera, 2017; Bai et al., 2017). Our model can also predict the abrupt uplift produced by the Papatea fault, which has not been reproduced in other published models. In addition to reproducing the complicated surface displacement, our model can also explain major features in both the strong motion and teleseismic waves. Moreover, our model successfully predicts the tsunami waveforms (Fig. 5c). While Bai et al. (2017) and Furlong and Herman (2017) attributed the tsunami sources to the shallow slip on the megathrust, our simulations indicate that the faults splay off from the subduction interface caused the uplift and contributed mostly to the tsunami sources. Our joint analysis shows that ana-

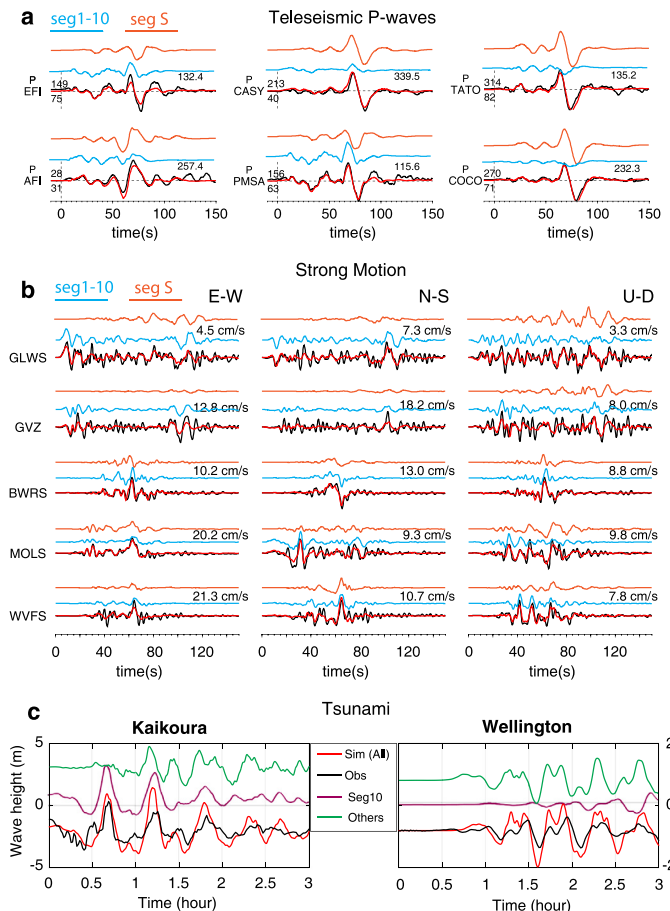


Fig. 5. Fit of selected seismic and tsunami data. **a.** Teleseismic P-wave fits between the data (black) and synthetics (red). Synthetics are decomposed into contributions from segments (Seg) 1–10 (blue) and Seg S (orange). The name of the station is indicated at the beginning of the data along with distance (lower) and azimuth (upper) in degrees. The maximum amplitude in the data is shown at the end of the trace in micrometers. **b.** Three-component strong-motion waveform fits for representative stations (see Fig. S1 for station locations). The black is data and the red is synthetic from the preferred kinematic model decomposed into the contribution from Seg 1–10 (blue) and Seg S (orange). The station names are indicated at the beginning of the E–W component with the maximum amplitude in the data shown at the end of each component. **c.** Tsunami waveform fits at the Kaikōura and Wellington station. The data is presented in black and synthetics from the preferred model are in red along with the contribution from Seg 10 (purple) and the rest of the fault segments (green).

lyzing a single or incomplete datasets may not have enough resolution to achieve a comprehensive understanding of an earthquake, particularly for an extreme event like the Kaikōura earthquake.

Nevertheless, we still could not exclude the possibility that the slip occurred on the Kekerengu fault and Jordan Thrust fault with a possible listric plane connecting to the plate interface or to a shear zone above the interface. Such a scenario has been recently proposed by Cesca et al. (2017). They use a three-segment finite fault model to fit the seismological and geodetic data, and suggest that large portion of the slip occurred on a crustal thrust fault kinematically connecting the overlying strike-slip faults, which is similar to our fault segment representing the interface but about 5 km shallower. They claim that no slip on the interface is required as they find that relocated thrust-faulting aftershocks mostly occurred above the slab (Cesca et al., 2017). But this interpretation cannot exclude the possibility that the strain on the plate interface has been released during the mainshock with aftershocks occurred in a shear zone slightly above the interface. Resolving the 5-km depth differences between our model and theirs would require more detailed analysis and will properly subject to stronger non-uniqueness in the solution. This is because the sensitivity of geodetic data decreases very fast with depth and nearby seismic observations are insufficient to determine earthquake locations and mechanisms to the resolution that is needed. Different interpretations using similar datasets demonstrated the non-uniqueness of finite fault model inversions. In a follow-up study, we may better resolve the fault geometry and rheology beneath the northern South Island by probing characteristics of the postseismic deformation.

4. Discussion and conclusions

Simultaneous rupturing of the subduction interface and its splay faults (Fig. 6) explains the highly-segmented uplift pattern along the coast, which may result from the slip partitioning among the high-dipping angle splay faults (Fig. 6). During the earthquake, the block bounded by two fault systems parallel to the coast was likely squeezed out by the oblique westward slip south of the Kekerengu fault (Fig. 2a). When the mini-block south of the Jordan Thrust fault and the upper Kowhai fault was extruded by the westward motion (Figs. 2a and 6), the slip was partitioned into uplifting and southeastward motion between the Kaikōura Peninsula and the Papatea fault (Fig. 2a). By contrast, the region near the Hope fault shows minor horizontal motion, but only uplifting to the south. This is because of the nearly fault-perpendicular up-dip thrust along its subvertical fault plane. The southward motion between the Papatea and Kekerengu Faults can be explained by the shallow northwest-dipping ($\sim 45^\circ$) of the Jordan Thrust fault during the extrusion, but it can be alternatively interpreted as a result of thrust faulting occurred offshore (Clark et al., 2017). Distinguishing these two kinds of models will need evidence from seafloor surveys after the earthquake. The vertical coastal displacement pattern demonstrates that geomorphological features in a single event, such as stepped river terraces, can be overprinted on

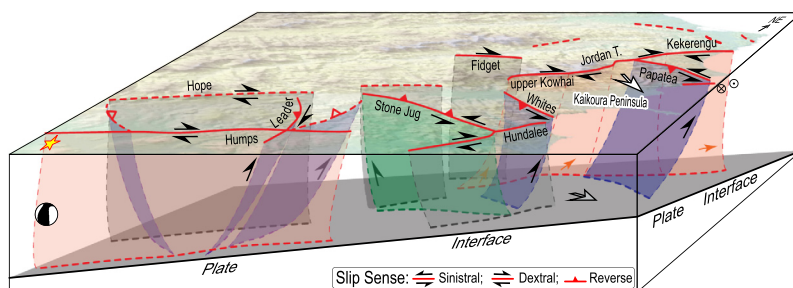


Fig. 6. A cartoon showing the proposed 3D configuration of the subduction interface and overlying faults. The beach ball indicates the hypocenter of the mainshock and the yellow star shows the epicenter location. Light red and gray planes show right-lateral faults that are generally parallel to the coastline with near-vertical geometry. Light purple and green planes show high-angle reverse faults that splay off the interface. The interaction among these faults caused their near simultaneous rupture during the Kaikōura earthquake. Note that the horizontal and vertical planes are not on the same scale.

smooth vertical displacement produced by slip on the subduction interface. Such overprinted deformation driven by aforementioned simultaneous rupture slip within a complex multi-splay fault system will significantly change how the coastal uplift rate is interpreted.

The pattern of vertical displacement changed the coastal landscape and also caused spatial variations in the amplitude of the tsunami. We used the vertical deformation predicted by our joint inversion model to simulate tsunami waveforms at four tide gauge stations (Fig. S1). To first order, the simulation results fit well in both the timing and the shape of the recorded tsunami waveforms at the Kaikōura and Wellington stations (Fig. 5c). Particularly, as the abrupt vertical motion associated with the Papatea fault is closest to the ocean, it plays the largest role in generating the offshore uplift and the distribution of tsunami waveforms (Fig. 4b and Fig. S8). The decomposition of the contribution from the Papatea and other faults also shows that the first 20-minute negative pulse at the Kaikōura station is well reproduced due to the uplift caused by the Papatea fault, and that rupture to the northeast contributed more to the tsunami waves recorded at the Wellington station (Fig. 5c).

Our analysis reveals simultaneous rupture of the plate interface and overlying faults with various dip angles during the 2016 Kaikōura earthquake event. Our interpretation is supported by comprehensive datasets comprising rupture geometry, space geodesy, seismograms and tsunami waveform records. The joint inversion of geodetic and seismic waveform data shows that the largest moment release took place about 65 s after the beginning of the rupture, corresponding to simultaneous rupture on both the subduction interface and the upper crustal splay faults. Our model successfully predicted the tsunami waveform records in directions both away and towards the rupture, demonstrating that rupturing the splay faults can enhance vertical displacements along the coast, and therefore may generate more energetic tsunamis during megathrust earthquakes than those only rupturing the plate interface. Therefore, retrieving the location and geometry of faults overlying the subduction interface may improve early warning and characterization of tsunami hazard.

Acknowledgements

The Sentinel-1A/B images are provided by the European Space Agency. The ALOS-2 images were provided by JAXA under the ALOS-2 RA4 Research Project 1413. We thank the NIWA for providing public-available 250-m-resolution bathymetry, and GNS Science for providing active fault database, earthquake rupture maps and reports, continuous GPS data, and strong motion waveform data. T.W., S.W., X.S., Q.Q., L.L., D.P. and S.B. thank the support from the Earth Observatory of Singapore (EOS), Nanyang Technological University through its funding from the National Research Foundation Singapore and the Ministry of Education - Singapore under the Research Centers of Excellence initiative. S.W. is supported by EOS startup fund M4430240.B50. T.W., D.P. and S.B., were also supported by the National Research Foundation of Singapore under the NRF Fellowship scheme (National Research Fellow Award NRF-NRFF2013-04) and Ministry of Education - Singapore Academic Research Fund Tier 1 RG181/16. X.S. thanks EOS fund M4430214.B50. This work comprises Earth Observatory of Singapore contribution 160. We thank Y. Wang, J. Moore, M. Hamahashi and P. Tapponnier at EOS for discussions. We thank two anonymous reviewers for their comments and suggestions.

Appendix A. Supplementary material

Supplementary material related to this article can be found online at <https://doi.org/10.1016/j.epsl.2017.10.056>.

References

- Argus, D.F., Gordon, R.G., 1991. No-net-rotation model of current plate velocities incorporating plate motion model Nuvel-1. *Geophys. Res. Lett.* 18, 2039–2042.
- Avouac, J.P., Meng, L.S., Wei, S.J., Wang, T., Ampuero, J.P., 2015. Lower edge of locked Main Himalayan Thrust unzipped by the 2015 Gorkha earthquake. *Nat. Geosci.* 8, 708–711.
- Bai, Y.F., Lay, T., Cheung, K.F., Ye, L.L., 2017. Two regions of seafloor deformation generated the tsunami for the 13 November 2016, Kaikoura, New Zealand earthquake. *Geophys. Res. Lett.* 44 (13), 6597–6606.
- Barker, D.H.N., Sutherland, R., Henrys, S., Bannister, S., 2009. Geometry of the Hikurangi subduction thrust and upper plate, North Island, New Zealand. *Geochem. Geophys. Geosyst.* 10.
- Bouchon, M., Vallee, M., 2003. Observation of long supershear rupture during the magnitude 8.1 Kunlunshan earthquake. *Science* 301, 824–826.
- Cesca, S., Zhang, Y., Mouslopoulou, V., Wang, R., Saul, J., Savage, M., Heimann, S., Kufner, S.-K., Oncken, O., Dahm, T., 2017. Complex rupture process of the Mw 7.8, 2016, Kaikoura earthquake, New Zealand, and its aftershock sequence. *Earth Planet. Sci. Lett.* 478, 110–120.
- Clark, K., Nissen, E., Howarth, J., Hamling, I., Mountjoy, J., Ries, W., Jones, K., Goldstien, S., Cochran, U., Villamor, P., 2017. Highly variable coastal deformation in the 2016 Mw 7.8 Kaikōura earthquake reflects rupture complexity along a transpressional plate boundary. *Earth Planet. Sci. Lett.* 474, 334–344.
- Duputel, Z., Rivera, L., 2017. Long-period analysis of the 2016 Kaikoura earthquake. *Phys. Earth Planet. Inter.* 265, 62–66.
- Eberhart-Phillips, D., Bannister, S., 2010. 3-D imaging of Marlborough, New Zealand, subducted plate and strike-slip fault systems. *Geophys. J. Int.* 182, 73–96.
- Ekstrom, G., Nettles, M., Dziewonski, A.M., 2012. The global CMT project 2004–2010: Centroid-moment tensors for 13,017 earthquakes. *Phys. Earth Planet. Inter.* 200, 1–9.
- Elliott, J.R., Jolivet, R., Gonzalez, P.J., Avouac, J.P., Hollingsworth, J., Searle, M.P., Stevens, V.L., 2016. Himalayan megathrust geometry and relation to topography revealed by the Gorkha earthquake. *Nat. Geosci.* 9, 174–180.
- Furlong, K.P., Herman, M., 2017. Reconciling the deformational dichotomy of the 2016 Mw 7.8 Kaikoura NZ earthquake. *Geophys. Res. Lett.* 44 (13), 6788–6791.
- Hamling, I.J., Hreinsdóttir, S., Clark, K., Elliott, J., Liang, C.R., Fielding, E., Litchfield, N., Villamor, P., Wallace, L., Wright, T.J., D'Anastasio, E., Bannister, S., Burbidge, D., Denys, P., Gentle, P., Howarth, J., Mueller, C., Palmer, N., Pearson, C., Power, W., Barnes, P., Barrell, D.J.A., Van Dissen, R., Langridge, R., Little, T., Nicol, A., Pettinga, J., Rowland, J., Stirling, M., 2017. Complex multifault rupture during the 2016 Mw 7.8 Kaikoura earthquake, New Zealand. *Science* 356.
- Harris, R.A., Day, S.M., 1999. Dynamic 3D simulations of earthquakes on en echelon faults. *Geophys. Res. Lett.* 26, 2089–2092.
- Hollingsworth, J., Ye, L.L., Avouac, J.P., 2017. Dynamically triggered slip on a splay fault in the Mw 7.8, 2016 Kaikoura (New Zealand) earthquake. *Geophys. Res. Lett.* 44, 3517–3525.
- Ji, C., Wald, D.J., Helmberger, D.V., 2002. Source description of the 1999 Hector Mine, California, earthquake, part I: wavelet domain inversion theory and resolution analysis. *Bull. Seismol. Soc. Am.* 92, 1192–1207.
- Kaiser, A., Balfour, N., Fry, B., Holden, C., Lichfield, M., Gerstenberger, M., D'Anastasio, E., Horspool, N., McVerry, G., Ristau, J., Bannister, S., Christophersen, A., Clark, K., Power, W., Rhoades, D., Massey, C., Hamling, I., Wallace, L., Mountjoy, J., Kaneko, Y., Benites, R., Van Houtte, C., Dellow, S., Wotherspoon, L., Elwood, K., Gledhill, K., 2017. The 2016 Kaikōura, New Zealand, earthquake: preliminary seismological report. *Seismol. Res. Lett.* 88, 727–739.
- Lane, E.M., Borrero, J., Whittaker, C.N., Bind, J., Chague-Goff, C., Goff, J., Goring, D., Hoyle, J., Mueller, C., Power, W.L., Reid, C.M., Williams, J.H., Williams, S.P., 2017. Effects of Inundation by the 14th November, 2016 Kaikōura Tsunami on Banks Peninsula, Canterbury, New Zealand. *Pure Appl. Geophys.* 174, 1855–1874.
- Langridge, R.M., Ries, W.F., Litchfield, N.J., Villamor, P., Van Dissen, R.J., Barrell, D.J.A., Rattenbury, M.S., Heron, D.W., Haubrock, S., Townsend, D.B., Lee, J.M., Berryman, K.R., Nicol, A., Cox, S.C., Stirling, M.W., 2016. The New Zealand active faults database. *N.Z. J. Geol. Geophys.* 59, 86–96.
- Litchfield, N., Benson, A., Bischoff, A., Hatem, A., Barrier, A., Nicol, A., Wandres, A., Lukovic, B., Hall, B., Gasston, C., Asher, C., Grimshaw, C., Madugo, C., Fenton, C., Hale, D., Barrell, D.J.A., Heron, D.W., Strong, D.T., Townsend, D.B., Noble, D., Howarth, J.D., Pettinga, J., Kearse, J., Williams, J., Manousakis, J., Mountjoy, J., Rowland, J., Clark, K.J., Pedley, K., Sauer, K., Berryman, K.R., Hemphill-Haley, M., Stirling, M.W., Villeneuve, M., Cockcroft, M., Khajavi, N., Barnes, P., Villamor, P., Carne, R., Langridge, R.M., Zinke, R., Van Dissen, R.J., McColl, S., Cox, S., Lawson, S., Little, T., Stahl, T., Cochran, U.A., Toy, V., Ries, W.F., Juniper, Z., 2017. 14th November 2016 M7.8 Kaikoura Earthquake. Summary Surface Fault Rupture Traces and Displacement Measurements (Version 3). GNS Science. <https://doi.org/10.21420/G21422RC21427C>.
- Litchfield, N.J., Van Dissen, R., Sutherland, R., Barnes, P.M., Cox, S.C., Norris, R., Beavan, R.J., Langridge, R., Villamor, P., Berryman, K., Stirling, M., Nicol, A., Nodder, S., Lamarche, G., Barrell, D.J.A., Pettinga, J.R., Little, T., Pondard, N., Mountjoy, J.J., Clark, K., 2014. A model of active faulting in New Zealand. *N.Z. J. Geol. Geophys.* 57, 32–56.

- Mountjoy, J.J., Barnes, P.M., 2011. Active upper plate thrust faulting in regions of low plate interface coupling, repeated slow slip events, and coastal uplift: example from the Hikurangi Margin, New Zealand. *Geochem. Geophys. Geosyst.* 12.
- Power, W., Clark, K., King, D., Borrero, J., Howarth, J., Lane, E.M., Goring, D., Goff, J., Chague-Goff, C., Williams, J., Reid, C., Whittaker, C., Mueller, C., Williams, S., Hughes, M., Hoyle, J., Bind, J., Strong, D., Litchfield, N., Benson, A., 2017. Tsunami runup and tide-gauge observations from the 14 November 2016 M7.8 Kaikōura earthquake, New Zealand. *Pure Appl. Geophys.* 178 (7), 2457–2473.
- Qiu, Q., Hill, E.M., Barbot, S., Hubbard, J., Feng, W.P., Lindsey, E.O., Feng, L.J., Dai, K.R., Samsonov, S.V., Tapponnier, P., 2016. The mechanism of partial rupture of a locked megathrust: the role of fault morphology. *Geology* 44, 875–878.
- Shi, X.H., Wang, Y., Jing, L.Z., Weldon, R., Wei, S.J., Wang, T., Sieh, K., 2017. How complex is the 2016 Mw 7.8 Kaikoura earthquake, South Island, New Zealand? *Sci. Bull.* 62, 309–311.
- Stirling, M.W., Litchfield, N., Villamor, P., Van Dissen, R., Nicol, A., Pettinga, J., Barnes, P., Langridge, R., Little, T., Barrell, D., 2017. The Mw 7.8 2016 Kaikōura earthquake: surface fault rupture and seismic hazard context. *Bull. N.Z. Soc. Earthqu. Eng.* 50, 73–84.
- Takada, Y., Fukushima, Y., 2013. Volcanic subsidence triggered by the 2011 Tohoku earthquake in Japan. *Nat. Geosci.* 6, 637–641.
- USGS, 2016. USGS, executive summary of M7.8 Amherst, New Zealand earthquake. <https://earthquake.usgs.gov/earthquakes/eventpage/us1000778i-executive>.
- Van Dissen, R., Yeats, R.S., 1991. Hope fault, Jordan thrust, and uplift of the Seaward Kaikoura Range, New Zealand. *Geology* 19, 393–396.
- Wei, S.J., Fielding, E., Leprince, S., Sladen, A., Avouac, J.P., Helmberger, D., Hauksson, E., Chu, R.S., Simons, M., Hudnut, K., Herring, T., Briggs, R., 2011. Superficial simplicity of the 2010 El Mayor-Cucapah earthquake of Baja California in Mexico. *Nat. Geosci.* 4, 615–618.
- Wesnousky, S.G., 2006. Predicting the endpoints of earthquake ruptures. *Nature* 444, 358–360.
- Williams, C.A., Eberhart-Phillips, D., Bannister, S., Barker, D.H.N., Henrys, S., Reyners, M., Sutherland, R., 2013. Revised interface geometry for the Hikurangi subduction zone, New Zealand. *Seismol. Res. Lett.* 84, 1066–1073.
- Zhang, H., Koper, K.D., Pankow, K., Ge, Z., 2017. Imaging the 2016 M_w 7.8 Kaikoura, New Zealand earthquake with teleseismic P waves: a cascading rupture across multiple faults. *Geophys. Res. Lett.* 44, 4790–4798.